

Neutron yields from 435 MeV/nucleon Nb stopping in Nb and 272 MeV/nucleon Nb stopping in Nb and Al

L. Heilbronn,¹ R. Madey,² M. Elaasar,^{2,*} M. Htun,^{2,†} K. Frankel,¹ W. G. Gong,³ B. D. Anderson,² A. R. Baldwin,² J. Jiang,^{2,‡} D. Keane,² M. A. McMahan,¹ W. H. Rathbun,¹ A. Scott,^{2,§} Y. Shao,^{2,||} J. W. Watson,² G. D. Westfall,⁴ S. Yennello,^{4,¶} and W.-M. Zhang²

¹Lawrence Berkeley National Laboratory, Berkeley, California 94720

²Kent State University, Kent, Ohio 44242

³MPI, Foehringer Ring 6, D-80805 Munich, Germany

⁴Michigan State University, East Lansing, Michigan 48824

(Received 23 February 1998; revised manuscript received 27 July 1998)

Neutron fluences were measured from 435 MeV/nucleon Nb ions stopping in a Nb target and 272 MeV/nucleon Nb ions stopping in targets of Nb and Al for neutrons above 20 MeV and at laboratory angles between 3° and 80°. The resultant spectra were integrated over angles to produce neutron energy distributions and over energy to produce neutron angular distributions. The total neutron yields for each system were obtained by integrating over the angular distributions. The angular distributions from all three systems are peaked forward, and the energy distributions from all three systems show an appreciable yield of neutrons with velocities greater than the beam velocity. Comparison of the total neutron yields from the two Nb+Nb systems suggests that the average neutron multiplicity decreases with decreasing projectile energy. Comparison of the total yields from the two 272 MeV/nucleon systems suggests that the total yields show the same dependence on projectile and target mass number as do total inclusive neutron cross sections. The data are compared with Boltzmann-Uehling-Uhlenbeck model calculations. [S0556-2813(98)05312-6]

PACS number(s): 25.75.-q, 25.75.Dw

I. INTRODUCTION

Neutron spectra produced by 435 MeV/nucleon Nb ions stopping in a Nb target and by 272 MeV/nucleon Nb ions stopping in Al and Nb targets were measured at the Lawrence Berkeley Laboratory's Bevalac facility. The spectra reported here are for neutrons with energies from 20 MeV up to twice the beam energy (in MeV/nucleon), and for laboratory angles between 3° and 80°. These measurements were motivated by the desire to provide some insight into the nature of the neutron spectra produced by interactions of high-energy heavy ions ($Z \geq 3$, referred to as HZE) present in galactic cosmic rays (GCR) with shielding materials used to protect humans engaged in long-term missions outside the geomagnetosphere. Data are useful also to the heavy-ion radiotherapy community, where the calculation of the dose delivered inside the patient must take into account the flux of neutrons produced by the interactions inside the patient.

Because there are essentially no free neutrons in primary GCR, the only significant source of neutrons is from interac-

tions of the primary GCR with shielding materials. The yield of neutrons behind thick shielding is especially important because (1) interactions of the primary GCR in those shields produce neutrons that make up a sizable fraction of the particles behind the shielding [1] and (2) neutrons have relatively high weighting factors in terms of their potential to inflict biological damage [2]. One calculation predicts that close to 50% of the dose equivalent behind shielding comprised of 50 g cm⁻² of Martian regolith comes from neutrons [1]. Although HZE particles make up just 1% of the GCR (with 87% protons and 12% alphas) [3], similar calculations have shown that approximately 16% of the neutron flux behind 50 g cm⁻² of water comes from the fragmentation of HZE; another 15% comes from interactions with GCR alpha particles, with the remainder from proton-induced interactions [4].

The transport models [4,5] used in the calculations mentioned above and in other similar calculations, such as Monte Carlo codes used in heavy-ion radiotherapy problems, need cross section data for input into the codes and thick-target data for verification of the models' output. Because GCR encompass a wide range of particles (from protons up to iron, with some flux of ions heavier than iron) and a wide range of kinetic energies (with most of the GCR flux contained between 100 and 2000 MeV/nucleon), the set of data needed by those models will need to cover a significant portion of the range of ions and energies present in GCR. Also, the data set will need to include targets that cover a broad range of possible shielding materials and tissue components. There are data sets of neutron production cross sections [6–11] from HZE interactions, and there are data on the production of neutrons from 177.5 and 160 MeV/nucleon alphas stopping in various targets [12]; however, there are

*Present address: Department of Physics, Southern University, New Orleans, LA 70126.

†Present address: CyberAccess, Incorporated, Valley View, OH 44125.

‡Present address: Picker International, Solon, OH 44139.

§Present address: Department of Physics, University of Wisconsin-Stout, Menomonie, WI 54751.

||Present address: Crump Institute for Biological Imaging, UCLA, Los Angeles, CA 90095-6948.

¶Present address: Department of Chemistry, Texas A&M University, College Station, TX 77843.

few, if any, data sets of neutrons produced by HZE (with $Z > 2$) interactions in stopping targets.

The data presented here are intended to describe the general nature of neutrons produced by the interactions of the heavier constituents of GCR in a stopping target. This description includes such properties as the angular and energy distributions, the total yields, and the dependence of the yield on target mass and projectile energy. Details of the experiment follow in Sec. II, with the data analysis and discussion in Secs. III and IV. Comparisons of the data with a model that uses Boltzmann-Uehling-Uhlenbeck- (BUU-) generated cross sections are in Sec. V.

II. EXPERIMENTAL DETAILS

The data presented here come from a neutron time-of-flight experiment that was done at the Bevalac Facility at Lawrence Berkeley Laboratory. This experiment was an adjunct to experiment E848H [13]. The choice of beams was dictated by the physics goals of the primary experiment, hence the choice of Nb for both 435 and 272 MeV/nucleon beams. Although Nb is not a significant component of GCR, the reaction mechanisms producing neutrons in the systems used here are typical of heavy-ion reactions in this energy domain, and as such, the data reported here can be used to test models that calculate neutron production from HZE GCR-like ions. The beam was delivered in 1-s-long spills every 6 s, with approximately 3×10^5 particles per spill on target. Two beam-defining scintillators were placed upstream from the target for the purpose of identifying beam particles focused on the target with a minimum divergence. A valid beam particle was defined by the coincidence between the two scintillators.

The data came from 14 neutron detectors placed between 3° and 80° in the laboratory. Each neutron detector was a 10.16-cm-thick rectangular slab of NE-102. All 14 detectors were 101.6 cm in height. The widths of the detectors varied from detector to detector. Table I lists the angle, dimensions, flight path, and solid angle of each detector. Each detector was placed such that the center of the detector was at the same height as the target. Pulse-height calibrations were carried out with a ^{228}Th source, a precision amplifier with a gain of 10, and attenuators with attenuation factors of 2, 5, and 10. The pulse-height response was linear and stable over the entire time of the experiment. Directly in front of each neutron detector was a 6.4-mm-thick NE-102 scintillator with a height and width slightly larger than the neutron detector. This scintillator was used to reject any charged particles from the target that were incident on the neutron detector.

A 1-cm-thick (8.57 g cm^{-2}) Nb target was used for the 435 MeV/nucleon run, and a 0.51-cm-thick (4.37 g cm^{-2}) Nb target and a 1.27-cm-thick (3.43 g cm^{-2}) Al target were used for the 272 MeV/nucleon runs. All the targets were thick enough to stop the beam. The targets were housed in a scattering chamber that had a thin Mylar window positioned between the target and neutron detectors.

III. DATA ANALYSIS

A. Neutron energy determination and flux corrections

Neutron energies were determined by measuring the time of flight between a signal from the beam particle telescope

TABLE I. Information on the position of the neutron detectors used in this experiment. All detectors are 10.16 cm thick. The flight paths are measured relative to the center of the detector.

Laboratory angle (deg)	Height (cm)	Width (cm)	Flight path (cm)	Solid angle (msr)
3.0	101.6	2.5	840.0	0.36
6.0	101.6	2.5	840.0	0.36
9.0	101.6	12.7	840.0	1.80
12.0	101.6	12.7	840.0	1.80
16.0	101.6	25.4	840.0	3.60
20.0	101.6	25.4	840.0	3.60
24.0	101.6	25.4	840.0	3.60
28.0	101.6	25.4	840.0	3.60
32.0	101.6	25.4	840.0	3.60
36.0	101.6	25.4	840.0	3.60
40.0	101.6	50.8	840.0	7.20
48.0	101.6	50.8	800.0	7.94
56.0	101.6	50.8	750.0	9.03
64.0	101.6	50.8	700.0	10.37
72.0	101.6	50.8	620.0	13.22
80.0	101.6	50.8	600.0	14.11

and a mean-timed [14] signal from the neutron detector. An absolute time scale in each one of the resulting 14 time-to-digital converter (TDC) spectra was determined by measuring the position of the prompt gamma-ray peak. The timing resolution for the 435 MeV/nucleon run, as measured by the width [full width at half maximum (FWHM)] of the prompt gamma-ray peak, varied from 0.8 to 1.4 ns depending on the detector used; the timing resolution increased for the 272 MeV/nucleon runs to values between 1.4 and 1.7 ns. The raw TDC data for each detector and each run were rebinned such that the minimum bin width was at least the size of the appropriate timing resolution. Energy spectra were then produced from the rebinned TDC spectra.

The detection efficiency of each neutron detector was calculated using the code of Cecil *et al.* [15]. Figure 1 shows the detection efficiency as a function of energy for the four sizes of detectors used in this experiment, with a pulse-height threshold of 10 MeV in equivalent-electron energy, which is equivalent to about 18 MeV in neutron energy.

Corrections to the data were needed also to adjust for the loss of neutron flux from the presence of scattering materials between the target and neutron detector. The amount of neutron flux lost by scattering was calculated with a code containing the appropriate neutron scattering cross sections [16–18] and scattering materials. There was a wall of plastic scintillators mounted on a wooden frame placed between the target and neutron detectors at forward angles, and just in front of the scintillator wall was a thin sheet of steel used for delta-ray suppression. Although the data from the scintillator wall are not presented in this analysis, those materials were present at all times and the loss of neutron flux through them must be taken into account. The air between the target and neutron detectors also contributed to the loss of neutron flux and was included in the flux-transmission calculations. Shown in Fig. 2 as a function of neutron energy is the fraction of neutron flux transmitted from the target to the detectors between 3° and 20°

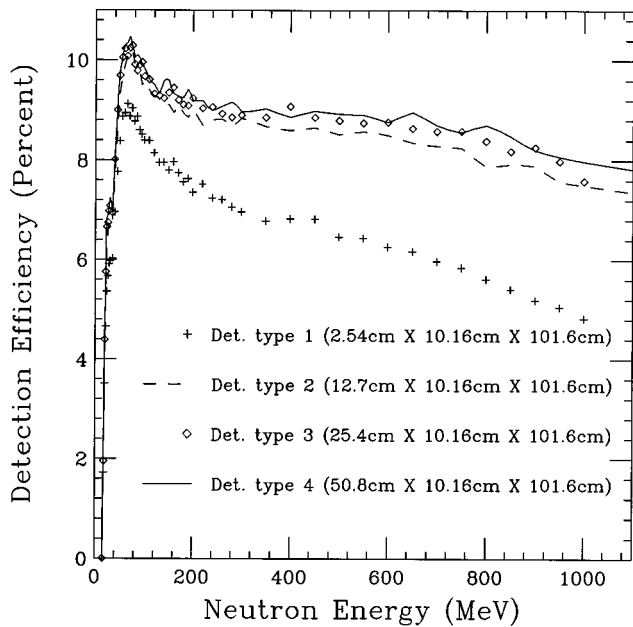


FIG. 1. Neutron detection efficiency for all four sizes of detectors used in the experiment. Efficiencies shown here were calculated using a pulse-height threshold of 10 MeV equivalent-electron energy.

(air+wood+plastic scintillator wall+steel+veto scintillator, shown by the solid line), 24° and 36° (air+wood+wall scintillator+veto scintillator, shown by dashed line), and 48° and 80° (air+veto scintillator, shown by the dotted line).

B. Background estimation

Because of the limited amount of beam time available for the measurements, background neutrons were not measured with shadow shields in place; instead, the background was estimated from particular regions in the TDC spectra where none of the events were generated by neutrons coming di-

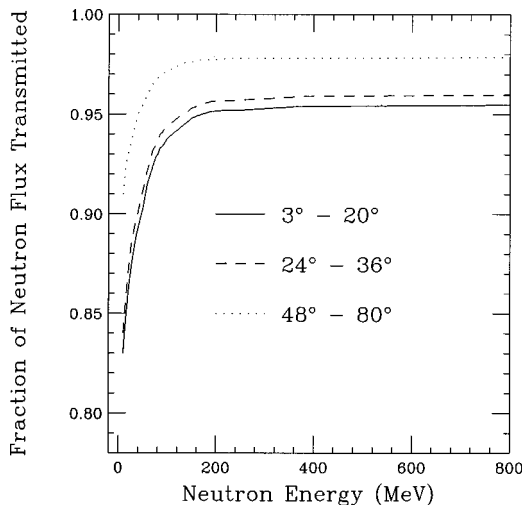


FIG. 2. Fraction of the neutron flux transmitted from the target to the neutron detector as a function of neutron energy. The solid line shows the transmitted fraction for detectors between 3° and 20°, the dashed line is for detectors between 24° and 36°, and the dotted line is for detectors between 48° and 80°.

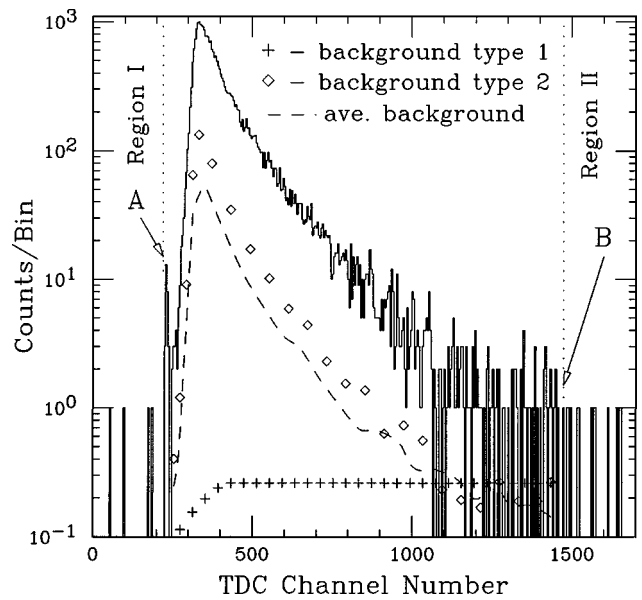


FIG. 3. TDC spectrum at 3° from the 435 MeV/nucleon Nb+Nb system, for a pulse-height threshold of 8 MeV equivalent-electron energy. The peak labeled “A” is due to prompt gamma rays. The other labels delineate regions used to determine the background, as explained in the text.

rectly from the target. Figure 3 shows a TDC spectrum for the detector at 3° gated on pulse heights above 8 MeV of equivalent electron energy. The peak labeled A is the prompt gamma-ray peak. Time increases from left to right; thus, all neutrons coming directly from the target will be to the right of the gamma-ray peak.

The counts to the left of the gamma-ray peak are from uncorrelated, out-of-time events. One source of these out-of-time events is cosmic rays that strike the neutron detector, but do not pass through the accompanying veto detector. The distribution of counts in this region (referred to hereon as “region I”) was flat in all cases. It is assumed that these out-of-time events will extend over the entire range of the TDC spectrum with a constant magnitude.

The channel marked B (channel number 1474) in Fig. 3 indicates the location in the TDC spectrum where the pulse-height threshold takes effect. Any counts to the right of channel B cannot come directly from the target because their time of flight has a corresponding energy that is below threshold. Instead, those events are out-of-time events which are also seen exclusively in region I, and target-induced background from room-scattered neutrons and gammas which are not present in region I; accordingly the average number of counts to the right of channel B (referred to as “region II”) should exceed the average number of counts in region I, which is the case for all detectors and for all pulse-height thresholds used. The distribution of counts in region II was flat for all detectors and thresholds used in the analysis.

There is no direct way to determine the shape and magnitude of the background spectrum between points A and B in Fig. 3; consequently, it is necessary to assume a background shape in that area and use the information available from regions I and II to determine the magnitude of that background. Two types of background shapes were assumed in this analysis, and the final background values were found by averaging over the two types.

One of the background shapes is similar to the one used in Ref. [12] and is shown with + symbols in Fig. 3; this type-I background is assumed to be flat (with a magnitude equal to the average number of counts in region II) from the threshold channel to the channel that corresponds to the flight time for a floor-scattered neutron coming from the target, with an energy equal to that of the high-energy peak in the TDC spectrum. The background is then assumed to decrease linearly from the floor-scattered channel down to the gamma peak position. The magnitude of the background at the gamma peak position is equal to the average number of counts in region I.

The second type of background, which applies to neutrons coming from the target that scatter from the floor, ceiling, and walls into a particular detector, assumes a shape to be the same as the measured spectrum; also, the background spectrum would be shifted along the x axis because the flight paths for background neutrons are longer than for neutrons coming directly from the target. Thus, for a particular neutron detector, the second type of background is calculated by (1) taking the measured TDC spectrum of that detector and multiplying it by a fixed percentage and then (2) shifting the TDC channel number to account for the longer flight times of room-scattered neutrons. The amount of the shift was calculated for the flight path of a neutron scattered from a point on the floor halfway between the target and the neutron detector. The fixed percentage was determined by setting the average number of counts in the assumed background TDC spectrum in region II equal to the average number of counts in region II of the measured TDC spectrum, where all the events in region II are background events. The fixed percentages varied from 5% to 15%, depending on the detector and reaction system used. An estimate of the background from floor-scattered neutrons was obtained by considering elastic scattering in a floor target one mean free path thick and assuming that the flux of neutrons incident on the floor is the same as that on a neutron detector. According to this estimate, the counts in the TDC spectra from floor scattering vary from 0.5% (for scattering off of a 1-m-wide strip of floor between the target and the detector at 80°) to 7% (for scattering of a 5-m-wide strip of floor between the target and the detector at 3°) of the total number of counts in the TDC spectra for the 435 MeV/nucleon system. For the 272 MeV/nucleon systems, the percentages for the same conditions parenthetically referred to above increased to 1% and 10%, respectively. Neutron scattering from other materials in the room gives additional contributions to the background. The open symbols in Fig. 3 show the type-2 background.

As can be seen in Fig. 3, the type-1 and type-2 backgrounds serve as the lower and upper bounds, respectively, in the background estimation. The dashed line in Fig. 3 shows the averaged-background contribution to that spectrum. The background contribution was greatest at the lowest energies (20–30 MeV), where the background contributions varied between 7% for the detector at 72° and 32% for the detector at 3° . The disparity between the two types of backgrounds is greatest for the highest-energy neutrons, where the magnitudes of the backgrounds varied by as much as a factor of 1000 at the forward angles; although this disparity is large, the uncertainty in the background at these points

contributed only 6–8 % in the overall uncertainty in the neutron spectra there.

IV. EXPERIMENTAL RESULTS

A. Double differential spectra

Neutron energy spectra were generated by first taking the raw TDC spectra, such as the spectrum shown in Fig. 3, and subtracting the background counts in each channel, using the averaged background described in Sec. III B. Next, each TDC channel value was converted to an energy, and then the number of counts in each energy bin was corrected for detection efficiency and flux transmission (see Sec. III A), using the calculations shown in Figs. 1 and 2. No parametrization of the detection efficiency and flux transmission was used; instead, an interpolation between points was used when necessary.

In addition to neutrons produced by interactions of the primary ion in the target, neutrons are also produced by interactions of secondary fragments in the target and outside the target. For neutrons produced by secondaries in the target, only neutrons on a direct path into the detector will be present in the spectra after correcting for background counts, as is the case for neutrons produced by primary interactions. No correction to the spectra has been made for neutrons from secondary fragments interacting in the target; however, these neutrons, as estimated in Sec. V, contribute no more than 10% to the reported spectra. In the case of neutrons produced by secondary interactions outside the target, the situation is more complicated because the relative position between the interaction point and the neutron detectors can be much different than in the case of primary and secondary interactions in the target. To first order, though, we assume that room-scattered neutrons from secondary interactions outside the target are eliminated in the background subtraction and that only neutrons emitted directly towards the neutron detectors are present in the spectra after correcting for background. Then, using a range-energy calculation, we determine which secondary fragments escape the target and at what energies they escape. Using air as the medium outside the target and using an energy-dependent geometric cross section formula [19–21], we then determine the percentage of secondary fragments that undergo a nuclear interaction. Based on this calculation, it is estimated that secondary interactions outside the target contribute no more than 5% to the reported spectra.

Shown in Figs. 4, 5, and 6 are neutron-energy spectra for the 435 MeV/nucleon Nb+Nb system, the 272 MeV/nucleon Nb+Nb system, and the 272 MeV/nucleon Nb+Al system, respectively. The uncertainties shown in the figures include the statistical uncertainties and the uncertainties from background subtraction. Scale uncertainties resulting from corrections for detection efficiency and flux transmission are not shown. Error bars are omitted when the uncertainty is smaller than the size of the plotting symbol. Spectra are shown for the detectors at 3° , 9° , 16° , 28° , 48° , and 80° . (A complete listing of the spectra from all 14 detectors is available in Lawrence Berkeley National Laboratory Report No. LBNL-41429.) The yields in these stopping-target spectra are expressed in units of the number of neutrons per MeV per unit solid angle per incident Nb ion. In all cases, the low-energy threshold was 20 MeV. The solid lines shown in

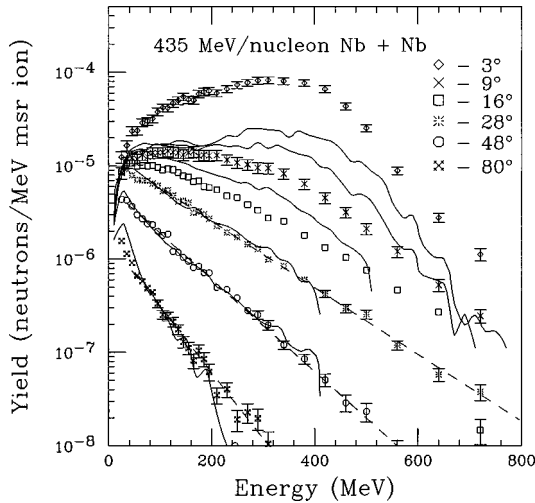


FIG. 4. Neutron-energy spectra from the 435 MeV/nucleon Nb+Nb system at 3°, 9°, 16°, 28°, 48°, and 80°. The data are shown by the symbols indicated in the plot. The solid lines are from a calculation of the data described in Sec. V, and the dashed lines come from a fit to the data using Eq. (1). Error bars have been suppressed where the plotted size of the uncertainty is less than the size of the plotting symbol.

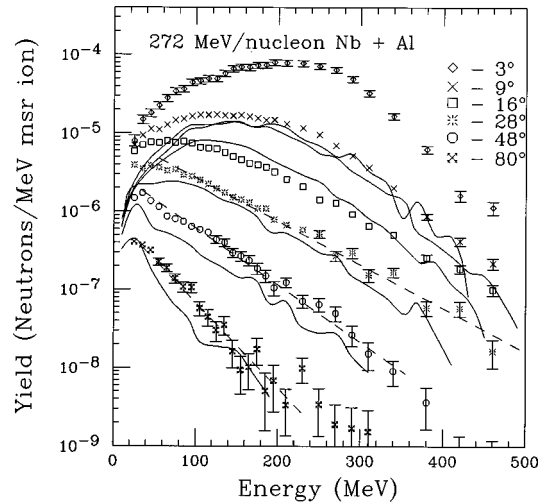


FIG. 6. Neutron-energy spectra from the 272 MeV/nucleon Nb+Al system at 3°, 9°, 16°, 28°, 48°, and 80°. The data are shown by the symbols indicated in the plot. The solid lines are from a calculation of the data described in Sec. V, and the dashed lines come from a fit to the data using Eq. (1). Error bars have been suppressed where the plotted size of the uncertainty is less than the size of the plotting symbol.

Figs. 4–6 represent BUU calculations. The details of those calculations are described in Sec. V. The dashed lines are a parametrization of the large-angle data, as explained later in this section.

Projectile fragmentation is the dominant mechanism for the production of neutrons at forward angles [22,23], as can be seen in Figs. 4–6 by the relative abundance of high-energy neutrons at those angles. One striking difference between the forward-angle spectra from stopping and thin targets is that the stopping-target spectra show a broad peak of projectilelike neutrons extending from about one-third of the

beam energy per nucleon up to an energy approximately 10–20% above the incident beam energy per nucleon, whereas thin-target forward-angle spectra show a much narrower peak centered near the incident beam energy per nucleon (see, for example, Refs. [6,24]). The difference arises from the fact that the interactions in the stopping target occur over a range of projectile energies extending from the incident beam energy per nucleon down to energies reached just before stopping in the target, while the thin-target reactions occur essentially over one projectile energy. Based on the assumption that the deviation of the spectral shapes from a straight exponential falloff is due primarily to projectilelike neutrons, contributions to the spectra from projectilelike neutrons can be seen qualitatively out to 9° in Fig. 4 and out to 16° in the 272 MeV/nucleon systems.

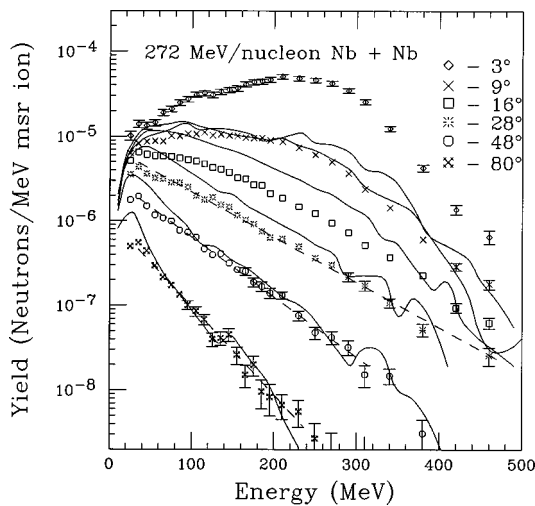


FIG. 5. Neutron-energy spectra from the 272 MeV/nucleon Nb+Nb system at 3°, 9°, 16°, 28°, 48°, and 80°. The data are shown by the symbols indicated in the plot. The solid lines are from a calculation of the data described in Sec. V, and the dashed lines come from a fit to the data using Eq. (1). Error bars have been suppressed where the plotted size of the uncertainty is less than the size of the plotting symbol.

At larger angles ($\theta \geq 28^\circ$) the spectra in all three cases are dominated by neutrons coming from the decay of the overlap region, or “mixing” region, of projectile and target nucleons. The spectra there show the same characteristics of particle production from the overlap region as seen in thin-target spectra [6,24], such as the exponential falloff with energy and the increase in the steepness of the slopes as the laboratory angle increases. As with thin-target spectra, the large angle stopping-target spectra can be represented with a simple exponential of the form

$$y = N \exp(-E_n / \langle E_0 \rangle), \tag{1}$$

where y is the number of neutrons per MeV per unit solid angle per incident ion at a particular angle and neutron energy E_n , N is a normalization constant, and $\langle E_0 \rangle$ is the slope parameter. Because interactions in the stopping target occur at all projectile energies from the incident energy on down, $\langle E_0 \rangle$ is not a parameter that describes the interactions at one particular projectile energy (as is the case when thin-target data are fitted with the same form of exponential [25]), but is rather a weighted average of the slope parameters over the

TABLE II. Values of the slope parameter $\langle E_0 \rangle$ used in Eq. (1) to fit the spectra for the systems and angles indicated. The fits are shown as dashed lines in Figs. 4–6. Here $\langle E_0 \rangle$ is in units of MeV.

	Nb+Nb 435 MeV/nucleon	Nb+Nb 272 MeV/nucleon	Nb+Al 272 MeV/nucleon
28°	121±7	81±6	77±5
48°	88±5	61±4	60±4
80°	62±4	42±3	40±3

entire range of interactions. Table II shows the values of $\langle E_0 \rangle$ for the systems and angles indicated. The uncertainties in Table II were determined by holding N constant at its best-fitted value and varying $\langle E_0 \rangle$ in the fitting procedure in order to find the two values of $\langle E_0 \rangle$ where $\chi^2 = \chi_{\min}^2 + 1$ [26] (where χ^2 is the deviation between the data and fitting function using the method of least squares, and χ_{\min}^2 is the minimum value of the deviation). The difference between the two values of $\langle E_0 \rangle$ where $\chi^2 = \chi_{\min}^2 + 1$ is then taken to be 2 times the uncertainty in $\langle E_0 \rangle$. The dashed lines in Figs. 4–6 show the fits to the data using Eq. (1). Comparison of the large-angle spectra from 435 MeV/nucleon system and the 272 MeV/nucleon systems shows steeper slopes (smaller values of $\langle E_0 \rangle$) in the lower-energy systems, which is consistent with the systematics found in the analyses of thin-target heavy-ion data (see Fig. 2 of Ref. [25], and references contained therein). A similar comparison between the two 272

MeV/nucleon systems shows that the mass of the target makes no significant difference on the spectral slopes at large angles.

B. Energy distributions

Because neutrons coming from the decay of a targetlike source dominate the spectra at low energies and at large angles, much of the contribution from targetlike neutrons is missing in the three spectra; the reason is the relatively high (20 MeV) neutron-energy threshold of the spectra and the relatively forward placement ($\theta \leq 80^\circ$) of the neutron detectors. The significance of the missing targetlike neutrons can be seen in the left-hand plots in Fig. 7 which show the energy-dependent neutron yields for all three systems after summing the experimental neutron spectra at all 14 angles over an angular range from 0° to 90° . The data are expressed in units of the number of neutrons per MeV per incident Nb ion. For all three systems, the spectra fall off with increasing neutron energy. Although the yield below threshold cannot be determined, the trend of the data shows that there is potentially a large yield of mostly targetlike neutrons below threshold. This point is important to consider when total neutron yields are extracted (see Sec. IV D below) from these data.

C. Angular distributions

The right-hand plots in Fig. 7 show the angular distributions for neutrons above 20 MeV found by summing the

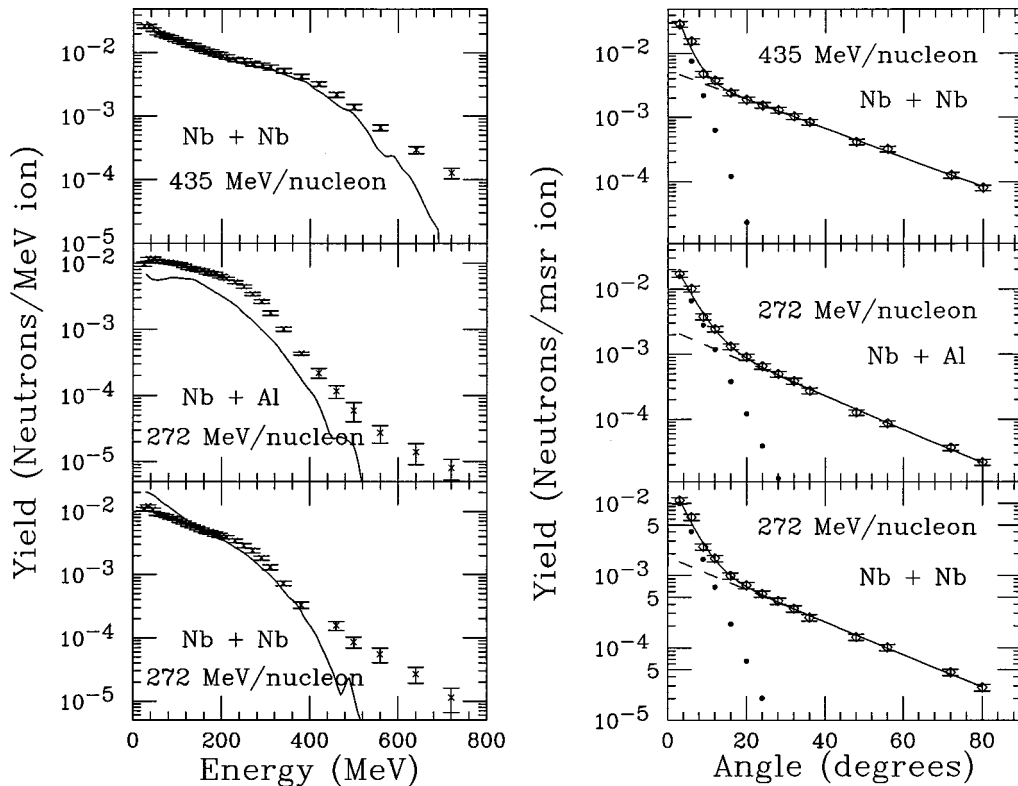


FIG. 7. The plots on the left side show the energy distributions of neutrons above 20 MeV from the systems indicated in each plot. The solid lines in the left-hand plots show a calculation of the data using a method described in Sec. V. The plots on the right side show the angular distributions of neutrons above 20 MeV from all three systems. The solid lines in the right-hand plots show a fit to the data using Eq. (2) of the text. The dotted and dashed lines show the contributions from each component of Eq. (2).

TABLE III. Fit parameters from Eq. (2) for all three systems. The angle θ in Eq. (2) is in units of degrees.

	Nb+Nb 435 MeV/nucleon	Nb+Nb 272 MeV/nucleon	Nb+Al 272 MeV/nucleon
a_1 (n /MeV incident ion)	$(5.4 \pm 0.5) \times 10^{-3}$	$(1.79 \pm 0.18) \times 10^{-3}$	$(2.44 \pm 0.25) \times 10^{-3}$
a_2 (1/deg)	$(5.2 \pm 0.2) \times 10^{-2}$	$(5.2 \pm 0.2) \times 10^{-2}$	$(5.9 \pm 0.2) \times 10^{-2}$
a_3 (n /MeV incident ion)	$(9.0 \pm 2.5) \times 10^{-2}$	$(2.4 \pm 0.6) \times 10^{-2}$	$(3.7 \pm 0.8) \times 10^{-2}$
a_4 (1/deg)	0.41 ± 0.05	0.29 ± 0.03	0.29 ± 0.03

double-differential energy spectra for all 14 angles. The angular distributions are expressed in units of the number of neutrons per unit solid angle per incident Nb ion. The uncertainties shown include a 10% scale uncertainty in the efficiency calculation and a 5% scale uncertainty in the attenuation calculation. Readily evident in all three spectra is that angular distributions are enhanced strongly in the forward direction. The solid lines show a fit to the data based on a superposition of two exponentials of the form

$$y = a_1 \exp(-a_2 \theta) + a_3 \exp(-a_4 \theta), \quad (2)$$

where a_1 , a_2 , a_3 , and a_4 are fit parameters and y is the number of neutrons per msr. Qualitatively, the two exponentials represent the separate contributions to the angular distributions from projectilelike neutrons and neutrons from the decay of overlap region.

The contributions to the fit from each exponential can be seen with the dotted [$a_3 \exp(-a_4 \theta)$] and dashed [$a_1 \exp(-a_2 \theta)$] lines. Table III shows the fit parameters for all three systems where the angle θ is expressed in degrees. The uncertainties in the fit parameters were determined by the same method used to find the uncertainties in the fit parameters in Table II. The contribution from forward-focused neutrons [$a_3 \exp(-a_4 \theta)$] shows a rapid falloff with laboratory angle, although the falloff is not as rapid in the 272 MeV/nucleon systems as it is in the 435 MeV/nucleon system. It is assumed that the forward-focused neutrons come primarily from the breakup of the projectile remnant, and the other neutrons [described with the other term in Eq. (2), $a_1 \exp(-a_2 \theta)$] come primarily from the decay of the overlap region. The point where there are equal contributions from projectilelike and overlap neutrons is around 9° for the 435 MeV/nucleon system and is around 12° for the 272 MeV/nucleon systems. The greater contribution from projectilelike neutrons at larger angles in the 272 MeV/nucleon systems is consistent with the decrease of the beam momentum per nucleon in those systems as compared to the 435 MeV/nucleon system. There is approximately a 25% change in momentum per nucleon going from the 435 MeV/nucleon system to the 272 MeV/nucleon system, and this leads to the observed 25% change in the point where there are equal contributions from the two sources (assuming there is no significant change in the transverse momentum between the two systems). It is interesting to note that the slope parameter for the overlap region (a_2) is the same for the two Nb+Nb systems, and only slightly higher in the Nb+Al system. The slope parameter for the forward-focused neutrons is the same for the two 272 MeV/nucleon systems.

D. Total yields

Table IV shows the total yields of neutrons above 20 MeV for all three systems expressed in units of the number of neutrons per incident Nb ion. The total yield is obtained by summing the 14 experimental points in the angular distribution over an angular range from 0° to 90° ; thus, the numbers in the second column of Table IV represent the number of neutrons above 20 MeV emitted in the forward 2π sr. The numbers in the third and fourth columns in Table IV are the number of neutrons above 20 MeV emitted in the first 45° and the first 10° , respectively. The last column in Table IV indicates the percentage of incoming Nb ions expected to undergo a nuclear interaction before stopping, as calculated by stepping the incident ion through successive layers of target and using the appropriate energy-dependent geometric cross section [19–21] at each layer. The uncertainties include the statistical (less than 2% for all systems) and scale (11% for all systems) uncertainties discussed above.

Dividing the total yields from Table IV by the corresponding expected fraction of interactions from Table IV yields average neutron multiplicities per interaction of 20 ± 2 for the 435 MeV/nucleon Nb+Nb system, 15 ± 2 for the 272 MeV/nucleon Nb+Nb system, and 11 ± 2 for the 272 MeV/nucleon Al+Nb system. Using the same calculation we used to estimate the fraction of incoming Nb ions that undergo a nuclear interaction, we estimate that 55% of the interactions in the 435 MeV/nucleon Nb+Nb system occur between 272 and 435 MeV/nucleon. With that assumption and using the neutron multiplicities from both the 435 and 272 MeV/nucleon Nb+Nb systems, we calculate that the average neutron multiplicity for interactions between 272

TABLE IV. Total neutron yields (in neutrons per incident ion) for the given systems and the given angular ranges. The numbers in the last column give the expected percentage of incoming ions that undergo a nuclear interaction, as determined from an energy-dependent total cross section calculation.

System	0° – 90°	0° – 45°	0° – 10°	% interacted
Nb+Nb				
435	4.5 ± 0.5	3.5 ± 0.4	1.3 ± 0.2	23
MeV/nucleon				
Nb+Nb				
272	1.7 ± 0.2	1.4 ± 0.2	0.54 ± 0.06	11.6
MeV/nucleon				
Nb+Al				
272	2.1 ± 0.3	1.9 ± 0.2	0.8 ± 0.1	19
MeV/nucleon				

and 435 MeV/nucleon is 24 ± 3 , as compared to 15 ± 2 for interactions from 272 MeV/nucleon on down. This indicates that the neutron multiplicity is increasing with increasing projectile energy. It is important to note that the measured total yields do not include neutrons with energies below 20 MeV and do not include neutrons emitted at angles greater than 90° . Those two restrictions exclude much of the yield from the target remnant and some of the yield from the overlap region; so a complete description of the dependence of the total yields and neutron multiplicities on incoming projectile energy is missing in this work.

Comparing the calculated average neutron multiplicities of the two 272 MeV/nucleon systems, we use the formalism developed by Madey *et al.* [27] to examine the dependence of average multiplicity in a stopping target on target mass. Using Eqs. (3) and (12) of Ref. [27],

$$M(\text{Nb}/\text{Al}, T > T_0) = \frac{\sigma_{\text{Al}}}{\sigma_{\text{Nb}}} * \left(\frac{A_{\text{Nb}}^{1/3} + A_{\text{Nb}}^{1/3}}{A_{\text{Al}}^{1/3} + A_{\text{Nb}}^{1/3}} \right)^{\alpha(T_0)}, \quad (3)$$

where $M(\text{Nb}/\text{Al}, T > T_0)$ is the ratio of the average Nb+Nb neutron multiplicity to the average Nb+Al neutron multiplicity above a neutron-energy threshold T_0 , A_{Nb} and A_{Al} are the atomic numbers of Nb and Al, σ_{Nb} and σ_{Al} are the total reaction cross sections for Nb+Nb and Nb+Al, respectively, and $\alpha(T_0)$ is the sole parameter that was fitted in Ref. [27]. The values for σ_{Nb} and σ_{Al} are calculated using the same geometric cross sections which were used in Table IV. From the work in Ref. [27], we use a value of 4.57 for $\alpha(T > 20 \text{ MeV})$. We then get $M(\text{Nb}/\text{Al}, T > 20 \text{ MeV}) = 1.42$, which is in agreement with the the the measured multiplicity ratio of $1.36 \pm 0.31 (= 15 \pm 2 / 11 \pm 2)$. This suggests that the relationship between total inclusive neutron cross section and the atomic numbers of the target and projectile found in Ref. [27] also holds true for total neutron yields from stopping targets.

One other work has looked at the target dependence on stopping-target neutron yields for alpha bombardment of various targets at 177.5 MeV/nucleon, and the authors have found that the integrated yields are independent of the target (0.5 neutrons per incident He ion) [12]. Within uncertainties, it can be said also that the total neutron yields are independent of the target in this work, although data below 20 MeV and at angles greater than 90° are needed here before a firm conclusion can be drawn in this regard.

As can be seen from the values in columns 3 and 4 of Table IV, much of the total yield is forward focused. Thirty percent of the flux in the Nb+Nb systems are contained within the first 10° , while 40% of the flux in the Nb+Al system is in the first 10° . About 80–90 % of the total flux between 0° and 90° is contained within the first 45° for all three systems.

V. BUU MODEL COMPARISONS

Boltzmann-Uehling-Uhlenbeck calculations have been compared with measured double-differential neutron cross sections; it is not possible, however, to take the output of such BUU calculations and directly compare them to stopping-target yields, such as the yields reported in this work. Stopping-target yields involve interactions over a wide

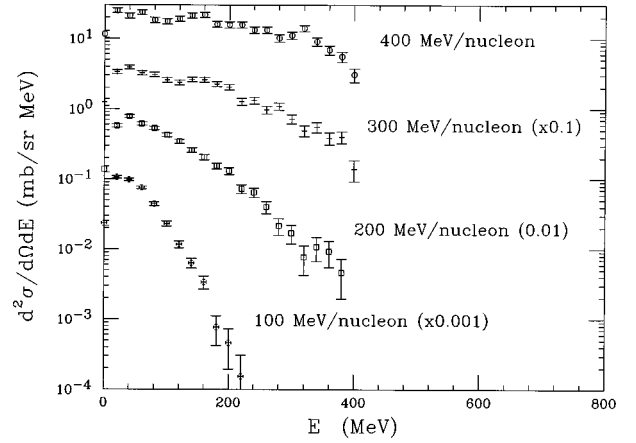


FIG. 8. BUU calculations of differential cross sections for neutron emission at 28° from Nb+Nb collisions at 400, 300, 200, and 100 MeV/nucleon. The spectra for the 300, 200, and 100 MeV/nucleon calculations are multiplied by the factors indicated in the plot.

range of projectile energies and may include a significant contribution from the interactions of secondaries within the target. Because these effects are not contained in any one BUU calculation, we employed a simple technique that builds up stopping-target yields from cross sections produced by BUU model calculations.

The first step was to transport the incident Nb ion through successive layers of the target. At each layer the energy loss of the incident Nb ion was calculated, along with the probability that the Nb ion underwent a nuclear interaction, as calculated using an energy-dependent geometric cross section [19–21]. Then a Monte Carlo simulation determined whether or not the Nb ion underwent a nuclear interaction; if so, the Nb energy at which the interaction took place was noted, and the Monte Carlo simulation used the neutron cross section calculated for that Nb energy to generate the multiplicity of neutrons resulting from the interaction, as well as the distribution of neutron energies and angles.

As a matter of practicality, BUU calculations of the cross sections were done at a few selected energies, and each calculation was used to represent the production cross sections for a range of Nb energies; for example, BUU calculations were run at 50, 100, 150, 200, 250, 300, 350, and 400 MeV/nucleon Nb energies in order to compare with the 435 MeV/nucleon data. The cross sections calculated at 50 MeV/nucleon were used to produce neutrons for any Nb ion up to 75 MeV/nucleon interacting in the target. The cross sections calculated at 100 MeV/nucleon were used whenever a Nb ion between 75 and 125 MeV/nucleon interacted in the target. Like the calculation done at 100 MeV/nucleon, all other calculations were used for a 50-MeV/nucleon-wide range of Nb interactions, except for the cross sections calculated at 400 MeV/nucleon, which were used for Nb interactions between 375 and 435 MeV/nucleon. In addition to using the method described above, in one case we also used an interpolation between BUU calculations to deduce cross sections at all interactions energies, and we found no difference in the results.

Figure 8 shows BUU cross sections for neutrons emitted at 28° from Nb-Nb collisions done at 400, 300, 200, and 100

MeV/nucleon. The calculations vary smoothly with projectile energy. The variance of the cross section at particular neutron energies was checked between calculations done at successive 50 MeV/nucleon intervals, and it was found that the cross sections varied by no more than a factor of 2 and, in general, varied by 20–50 %.

Once the appropriate neutron multiplicities, energies, and trajectories were determined, each neutron that was produced in the simulation was followed to see if it made it within the geometrical acceptance of any of the detectors used in the experiment. Neutron interactions in the target were neglected. A minimum of 10^7 Nb ions were transported through the target in each of the simulations. The simulated stopping-target yields were then normalized for the number of Nb ions and for the solid angle of the detector, allowing for a direct comparison with the experimental data.

The contribution to the neutron yield from interactions between secondary fragments and the target was estimated by allowing the incoming Nb ion to remain intact after an interaction, keeping the same energy it had at the time of the initial interaction. This “secondary” fragment was then transported through the rest of the target in the same manner as the original Nb ion. This method most likely overestimates the contribution from secondary fragments because it artificially regenerates the neutrons liberated in the initial interaction; however, including this estimate of the secondary component to the neutron flux increased the neutron yields by no more than 10% when compared to the flux calculated using primary interactions only.

In addition to producing protons and neutrons, the BUU calculation used here [28] also includes the production of deuterons. In all calculations an incompressibility modulus of $K=200$ was used.

Shown in Figs. 4–6 are spectra from all three systems along with the results from BUU calculations (solid lines). In the 435 MeV/nucleon Nb+Nb system (Fig. 4), the BUU model calculations compare well with the data at 28° and 48°, both in magnitude and in shape. At 80°, the BUU calculations do a good job predicting the magnitude of the spectrum, although it appears that the model predicts a slightly steeper slope than is observed with the data. At 9° and 16° the model does a good job of reproducing the shape of the spectra, but overpredicts the yields by 30% in both cases. At 3° the calculation again does a good job of reproducing the shape of the spectrum, but now it underpredicts the yield by a factor of 2.4. In the 272 MeV/nucleon Nb+Nb system (Fig. 5), the model is a reasonable representation of the data at 48° and 80°, matches the shape well, but overpredicts the yield by 50% at 28°, overpredicts the yield by a factor of 1.75 at 16°, matches the data at 9°, and underpredicts the yield by a factor of 2.2 at 3°. In the 272 MeV/nucleon Nb+Al data (Fig. 6), the model predicts a yield that falls off faster than the data as the energy decreases from 100 to 20 MeV at 3°, 9°, and 16°. Above 100 MeV, the spectral shapes at those angles are reproduced by the model calculation, although the normalizations are incorrect. At 3°, the model underpredicts the data by a factor of 3.7; at 9°, the yield is underpredicted by a factor of 1.6; and at 16°, the model overpredicts the yield by about 20%. At larger angles, the model underpredicts the yield by factors of 1.6 at 28°, 2.1 at 48°, and 1.6 at 80°. One clear trend in all three systems is

that the BUU calculations underpredict the 3° data (which are dominated by projectile fragmentation processes) by a large factor.

Shown in the energy-distribution plots in Fig. 7 (left-hand side) are comparisons with the data using BUU (solid line) calculations. The BUU calculation does well in reproducing the data at 435 MeV/nucleon. Integrating the BUU calculation over energy gives a total yield of 4.23 neutrons per incident ion, in close agreement with the experimental value of 4.45 neutrons per incident ion. The BUU calculation of the energy distribution in the 272 MeV/nucleon Nb+Al system reproduces the shape of the spectrum, but underestimates the yield. Integrating the BUU-generated energy distribution gives a total yield of 1.2 neutrons per incident ion, whereas the experimental value is 2.2 neutrons per incident ion. In the 272 MeV/nucleon Nb+Nb system, the BUU calculation overestimates the yield at energies below 100 MeV and underestimates the yield above 400 MeV. Integrating the BUU calculation over energy gives a total yield of 2.09 neutrons per incident ion, while the experimental total yield is 1.68 neutrons per incident ion. The disagreement between the model and data in the 272 MeV/nucleon Nb+Nb system indicates that the good agreement in the 435 MeV/nucleon Nb+Nb system may be fortuitous. Because the model overpredicts the yield below 100 MeV for the 272 MeV/nucleon systems, it must underpredict that same yield for ion energies ranging between 272 and 435 MeV/nucleon in order to match the data from the 435 MeV/nucleon system.

The disagreement between the data and model predictions is great enough to warrant further study; however, at this point it cannot be said whether the disagreement lies with (1) the BUU calculations of the cross sections or (2) the method of applying the BUU-generated cross sections to produce stopping-target yields. The very forward spectra (which are dominated by fragmentation processes and evaporation from the projectilelike remnant) that are calculated by BUU are sensitive to the cutoff density used in the calculation to determine whether a particle has been emitted or not. The value of the cutoff density used in the calculations here is 1/8 of normal nuclear density (taken to be 0.163 nucleons/fm³). Using a cutoff density of 1/16 of normal nuclear density led to a 20–30 % reduction in the yields at 3° and 9°, whereas it led to less than a 10% reduction in the yields at larger angles. Although the change in the magnitude of the yield at forward angles is significant when the cutoff density is reduced by a factor of 2, the change is not enough to reproduce the data at forward angles.

As noted above, the BUU model used here also produces deuterons. A BUU calculation which did not allow for the formation of composites was used to compare with 800 MeV/nucleon Nb+Nb neutron inclusive spectra [29]. There it was found that the BUU calculations overestimated the small-angle spectra, which was taken to show the importance of including cluster formation in such calculations. The inclusion of complex-particle formation into BUU model calculations has led to better comparisons between model calculations and cross section data; however, in order to compare model calculations with stopping-target data, complex particles formed in the calculation should be followed as they are transported through the remainder of the target to see if they undergo a nuclear interaction that produces any

neutrons or if they evaporate neutrons as they reach their final states. Not taking evaporation neutrons from projectile-like composites into consideration will lead to an underestimation of the small-angle yield, as has been observed in comparisons of quantum molecular dynamics (QMD) calculations with neutron inclusive spectra [29]. Because evaporation neutrons are not included in the comparisons shown here, the calculations underestimate the yield at forward angles.

No firm conclusions can be drawn here in regards to the disagreement between the data and BUU calculations because all or part of the disagreement may lie with the method that used the BUU calculations to produce stopping-target data. The BUU calculations will need to be compared directly to cross section data in order to firmly establish any shortcomings of using BUU-generated spectra in the method used here.

VI. CONCLUSIONS

Neutron angular and energy distributions, angle-integrated distributions, and energy-integrated distributions were measured for 272 and 435 MeV/nucleon Nb+Nb, and 272 MeV/nucleon Nb+Al interactions in stopping targets. Neutrons were measured from 20 MeV up to energies of twice the beam energy per nucleon. In all three systems contributions from projectile fragmentation can be seen as broad bumps in the forward-angle spectra. Spectra at larger angles obey an exponential behavior seen in similar thin-target experiments. The energy distributions in all three systems fall

off with increasing neutron energy. The total yields (integrated from 20 MeV on up and integrated from 0° to 90°) are 4.45 neutrons per incident ion in the 435 MeV/nucleon system, 1.68 neutrons per incident ion in the 272 MeV/nucleon Nb+Nb system, and 2.18 neutrons per incident ion in the 272 MeV/nucleon Nb+Al system. Comparison of the total neutron yields from the two Nb+Nb systems indicates that the average neutron multiplicity decreases with decreasing projectile energy, although data for neutron energies below 20 MeV and for angles greater than 90° are needed to draw a firm conclusion in that regard. Comparison of the total yields from the two 272 MeV/nucleon systems suggests that the total yields show the same dependence on projectile and target mass number as do total inclusive neutron cross sections. BUU model calculations did well in reproducing the large-angle data in the Nb+Nb systems. In the forward-angle Nb+Nb data and in the Nb+Al data, BUU calculations in general reproduced the spectral shapes, but either underpredicted or overpredicted the yield, depending on angle and system.

ACKNOWLEDGMENTS

This work was supported in part by the National Science Foundation under Grant Nos. PHY-98-96191, PHY-96-05207, PHY-91-07064, PHY-88-02392, and PHY-86-11210, the U.S. Department of Energy under Grant Nos. DE-FG89ER40531 and DE-AC03-76SF00098, and the National Aeronautics and Space Administration under NASA Grant Nos. L14230C and H29456D.

-
- [1] L. C. Simonsen and J. E. Nealy, NASA Technical Paper No. 3079, 1991.
- [2] *Annals of the ICRP—1990 Recommendations of the International Commission on Radiation Protection*, ICRP Publication No. 60 (Pergamon Press, Oxford, 1990), Vol. 21, Nos. 1–3.
- [3] *Guidance on Radiation Received in Space Activities*, NCRP Report No. 98 (National Council on Radiation Protection and Measurements, NCRP Publications, Bethesda, MD, 1989).
- [4] F. A. Cucinotta, NASA Technical Paper No. 3354, 1993.
- [5] J. W. Wilson, L. W. Townsend, W. Schimmerling, G. S. Khandelwal, F. Khan, J. E. Nealy, F. A. Cucinotta, L. C. Simonsen, J. L. Shinn, and J. W. Norbury, NASA Reference Publication No. 1257, 1991.
- [6] A. R. Baldwin, R. Madey, W.-M. Zhang, B. D. Anderson, D. Keane, J. Varga, J. W. Watson, G. D. Westfall, K. Frankel, and C. Gale, *Phys. Rev. C* **46**, 258 (1992).
- [7] W. Schimmerling, J. W. Kast, D. Ortendahl, R. Madey, R. A. Cecil, B. D. Anderson, and A. R. Baldwin, *Phys. Rev. Lett.* **43**, 1985 (1979).
- [8] R. A. Cecil, B. D. Anderson, A. R. Baldwin, R. Madey, W. Schimmerling, J. W. Kast, and D. Ortendahl, *Phys. Rev. C* **24**, 2013 (1981).
- [9] R. Madey, J. Varga, A. R. Baldwin, B. D. Anderson, R. A. Cecil, G. Fai, P. C. Tandy, J. W. Watson, and G. D. Westfall, *Phys. Rev. Lett.* **55**, 1453 (1985).
- [10] R. Madey, B. D. Anderson, R. A. Cecil, P. C. Tandy, and W. Schimmerling, *Phys. Rev. C* **28**, 706 (1983).
- [11] R. Madey, W. M. Zhang, B. D. Anderson, A. R. Baldwin, M. Elaasar, B. S. Flanders, D. Keane, W. Pairsuwan, J. Varga, J. W. Watson, G. D. Westfall, C. Hartnack, H. Stocker, and K. Frankel, *Phys. Rev. C* **42**, 1068 (1990).
- [12] R. A. Cecil, B. D. Anderson, A. R. Baldwin, R. Madey, A. Galonsky, P. Miller, L. Young, and F. M. Waterman, *Phys. Rev. C* **21**, 2471 (1980).
- [13] M. M. Htun, R. Madey, W. M. Zhang, M. Elassar, D. Keane, B. D. Anderson, A. R. Baldwin, J. Jiang, A. Scott, Y. Shao, J. W. Watson, K. Frankel, L. Heilbronn, G. Krebs, M. A. McMahan, W. Rathbun, J. Schambach, G. D. Westfall, S. Yennello, C. Gale, and J. Zhang, *Phys. Rev. C* (submitted).
- [14] A. R. Baldwin and R. Madey, *Nucl. Instrum. Methods* **161**, 439 (1980).
- [15] R. A. Cecil, B. D. Anderson, and R. Madey, *Nucl. Instrum. Methods* **161**, 439 (1979).
- [16] D. I. Garber, L. G. Stromberg, M. D. Goldberg, D. E. Cullen, and V. M. May, “Z=1 to 20,” Vol. I of “Angular Distributions in Neutron-Induced Reactions,” Brookhaven National Laboratory Report No. BNL-400, 1970.
- [17] D. I. Garber and R. R. Kinsey, “Neutron Cross Sections,” 3rd ed., Brookhaven National Laboratory Report No. BNL-324, 1976, Vol. II.
- [18] D. E. Cullen, R. D. Haight, R. J. Howerton, M. H. MacGregor, and S. T. Perkins, “Graphical Experimental Data for Supplemental Neutron-Induced Interactions,” Lawrence Livermore National Laboratory Report No. UCRL-50400, 1974, Vol. 8.

- [19] W. G. Gong, Ph.D. thesis, Michigan State University, 1992.
- [20] S. Kox, A. Gamp, C. Perrin, J. Arvieux, R. Bertholet, J. F. Bruandet, M. Buenerd, R. Cherkaoui, A. J. Cole, Y. El-Masri, N. Longequeue, J. Menet, F. Merchez, and J. B. Viano, *Phys. Rev. C* **35**, 1678 (1987).
- [21] L. W. Townsend and J. W. Wilson, *Phys. Rev. C* **37**, 892 (1988).
- [22] R. Serber, *Phys. Rev.* **72**, 1008 (1947).
- [23] A. S. Goldhaber, *Phys. Lett.* **53B**, 306 (1974).
- [24] R. Madey, W.-M. Zhang, B. D. Anderson, A. R. Baldwin, B. S. Flanders, W. Pairsuwan, J. Varga, J. W. Watson, and G. D. Westfall, *Phys. Rev. C* **38**, 184 (1988).
- [25] Z. Chen, C. K. Gelbke, W. G. Gong, Y. D. Kim, W. G. Lynch, M. R. Maier, F. Saint-Laurent, D. Ardouin, H. Delagrangé, H. Doubre, J. Kasagi, A. Kyanowski, A. Peghaire, J. Peter, E. Rosato, G. Bizard, F. Lefebvres, B. Tamain, J. Quebert, and Y. P. Viyogi, *Phys. Rev. C* **36**, 2297 (1987).
- [26] P. R. Bevington, *Data Reduction and Error Analysis for the Physical Sciences* (McGraw-Hill, New York, 1969), p. 242.
- [27] R. Madey, B. D. Anderson, R. A. Cecil, P. C. Tandy, and W. Schimmerling, *Phys. Rev. C* **28**, 706 (1983).
- [28] P. Danielewicz and G. F. Bertsch, *Nucl. Phys.* **A533**, 712 (1991).
- [29] R. Madey, W.-M. Zhang, B. D. Anderson, A. R. Baldwin, M. Elaasar, B. S. Flanders, D. Keane, W. Pairsuwan, J. Varga, and J. W. Watson, *Phys. Rev. C* **42**, 1068 (1990).